*EUROPEAN ORGANIZATION FOR NUCLEAR RESEARCH*

/afm CERN/PS/86-27 (AA)

# *A PLASMA LENS FOR FOCUSING HIGH ENERGY PARTICLES IN AN ACCELERATOR*

B. Autin and H. Riege
CERN, CH-1211 Geneva 23

E. Boggasch and K. Frank
Phys. Institut, Univ. of Erlangen-Nürnberg, D-852 Erlangen

L. De Menna and G. Miano
Ist. Elettr., Univ. of Naples, I-80138 Naples

## *ABSTRACT*

The high azimuthal magnetic field of a current carrying plasma column (z-pinch) can be used to collect and focus high energy charged particles in accelerators. The beam optics and the apparent advantages of such a linear lens compared with conventional focusing devices, like magnets and magnetic horns, are described. When a plasma lens shall be operated in routine accelerator runs, the physics of the plasma dynamics must be largely understood and the technology has to be mastered. The results of plasma dynamics measurements and of long term behaviour tests with a plasma lens for antiproton collection are reported. The problems of the plasma dynamics control and of the plasma-wall interaction are discussed in view of the envisaged beam optical performance.

(To be published in a Special Issue
of the IEEE TRANSACTIONS ON PLASMA SCIENCE
on Plasma-Based High-Energy Accelerators)

Geneva, Switzerland
November 1986

## Introduction

Intensive research on z-pinches as a potential plasma configuration to reach fusion conditions was going on twenty to thirty years ago. At this time a few attempts were made to use a z-pinch for focusing high energy charged particles[1]. A very powerful device, called plasma lens, was constructed, built and installed in the AGS synchrotron at BNL in 1965[2]. This plasma lens successfully focused secondary particles, but failed after a few hours of operation. No further applications of this kind have been pursued since, partly due to the almost total absence of general z-pinch research. Plasma instabilities and electrode problems favoured the transition of fusion research towards tokomak configurations.

Recently, the outstanding advantages of plasmas in accelerators, like very high acceleration field gradients and the excellent beam transport properties, have been recognized. Also the high poloidal magnetic field gradients, which can be achieved in a z-pinch plasma column, and the simultaneous focusing of energetic particles in both transverse planes are interesting, wherever a short focal length is needed. The negligible reabsorption of the high energy secondary particles to be focused in a low pressure plasma allows for current minimization by choosing the proper column length. Due to magnetic confinement mechanical stresses on the walls of the plasma vessel can be neglected.

The upgrading of the CERN antiproton source (ACOL) by a factor ten in antiproton intensity requires a very powerful collector lens. A plasma lens with a plasma column of 40 mm diameter and 300 mm length carrying a current of 400 kA seems the right device for this application. In order to avoid failures as experienced at BNL a research and development programme on a plasma lens for ACOL was started at CERN in 1983[3-4]. The ACOL plasma lens shall work for

more than $1.5 \cdot 10^6$ pulses at a repetition rate of 0.4 Hz. As for all known technical plasma devices the problems of plasma dynamics and of plasma wall interaction must be overcome to end up with a reliable instrument for accelerator operation.

Beam Optics

For high energy particles a plasma is nothing but a transparent conductor carrying a high current. The beam optics is thus the same in a plasma lens as in any axisymmetric lens and is determined by the particle motion in a radial plane. If the current density is uniform, the magnetic field varies linearly from a nul value on the axis to a maximum value on the outer radius $r_p$:

$$B = \mu_0 I_p/(2\pi r_p) \ , \qquad (1)$$

$I_p$ being the plasma current. The gradient of the field is proportional to the current density j:

$$G = \mu_0 j/2 \ . \qquad (2)$$

The configuration of the vectors $\vec{j}$ and $\vec{B}$, of the particle momentum $\vec{P}$ and of the restoring force $\vec{F}$ is represented in Fig. 1.

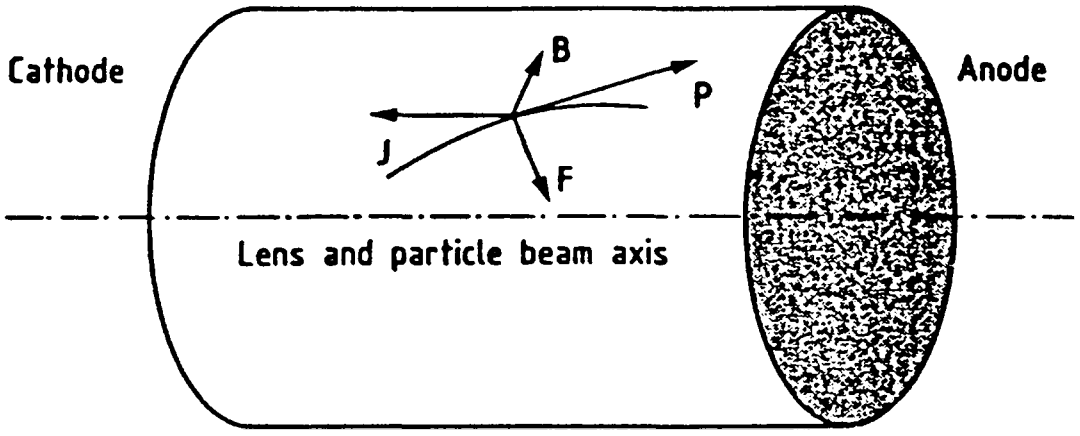


Fig. 1 - Antiproton deflection inside a current.

A beam is characterized by the distribution of its particles in the phase plane associated to the motion in a radial plane of the lens. In the case of a proton source or of an electron gun, the contour of the distribution is roughly elliptical but, for secondary particles like antiprotons, it depends on the geometry of the target (Fig. 2).

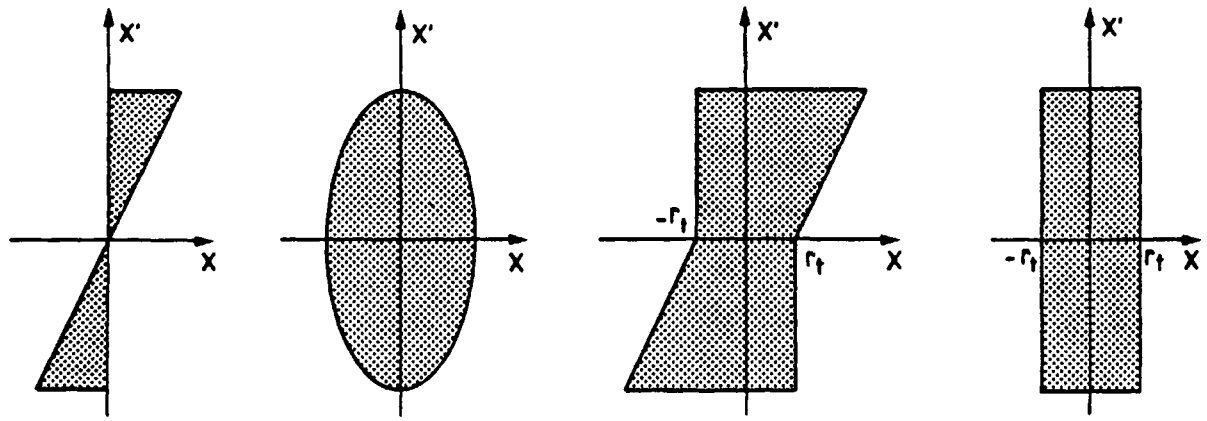


a) Thin and long b) Same as a, but submitted to an intense current c) Thick and long d) Flat disc

Fig. 2 - Phase-space beam emittance in cartesian coordinates at the end of various types of target.

Eventually the particles are injected into an accelerator or analysed in a detector; in both cases, the acceptance is defined as the window in phase space through which the particles can circulate or be observed. For an accelerator the acceptance is always elliptical and its image through a magnetic channel whose plasma lens is the end element is still an ellipse in linear optics. The lens ensures the transition between the target where the image of the acceptance ellipse is elongated along the momentum axis and the entry to a conventional channel of alternated gradient magnets where the divergence of the beam must be strongly diminished (Fig. 3). Due to the cylindrical symmetry, the beam is focused in all directions and the analogy between light and particle optics is complete.

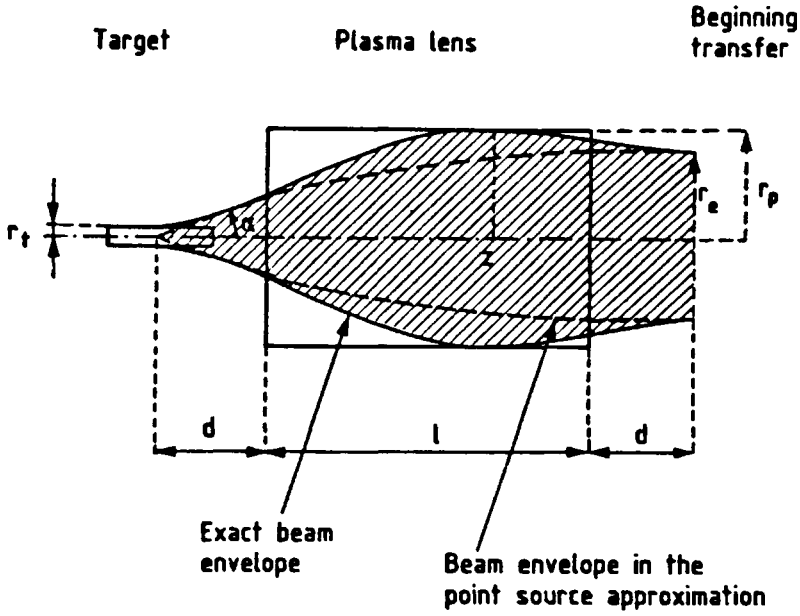


Fig. 3 - Optical system layout.

In practice, the radius of the beam at the target is small as compared to the lens radius and the calculations based on the transformation of a point source into a parallel beam give a good description of the lens. However, for the sake of generality, an envelope calculation will be presented and the point source will appear as a special case.

The optical system is limited by its two focal points. A ray emitted at the object focus exits parallel to the axis and an input ray parallel to the axis points towards the image focus at the exit from the lens. These two conditions joined to the emittance conservation impose a total transfer matrix of the type

$$\begin{pmatrix} 0 & f \\ -1/f & 0 \end{pmatrix} \tag{3}$$

for a convergent system. It is usual to define the focusing strength K of a quadrupole by the relation:

$$K = (e/p)G \ . \tag{4}$$

where e is the electron charge and p the particle momentum and to introduce the phase

$$\varphi = \sqrt{K}\, \ell \ , \tag{5}$$

$\ell$ being the length of the lens.

Reminding the transfer matrices of a quadrupole

$$\begin{pmatrix} \cos\varphi & (\ell/\sqrt{K})\sin\varphi \\ -\sqrt{K}\sin\varphi & \cos\varphi \end{pmatrix} \tag{6}$$

and of a straight section

$$\begin{pmatrix} 1 & d \\ 0 & 1 \end{pmatrix}, \tag{7}$$

the total transfer matrix has the wanted form if the distance d is chosen so that

$$d = 1/(\sqrt{K}\tan\varphi) \ , \tag{8}$$

the focal length is then

$$f = 1/(\sqrt{K}\sin\varphi) \ . \tag{9}$$

In order to determine the parameters $\ell$, d, $I_p$ and $R_p$, we consider the phase space ellipses at the foci as given and the phase as a variable. The expressions (8) and (9) can then be transformed into

$$\ell = (r_e/\alpha)\varphi\sin\varphi \tag{10}$$

$$d = (r_e/\alpha)\cos\varphi \ , \tag{11}$$

$\alpha$ being the input angle and $r_e$ the output radius. The expression of the focus ing strength as a function of the current is deduced from (2) and (4):

$$K = (e/p)(\mu_0/2\pi)I_p/r_p \ . \tag{12}$$

By substituting (10) and (12) into the very definition of the phase (5) it turns out that the current can take the form

$$I_p = (r_p/r_e)^2 I_0/\sin^2\varphi \ . \tag{13}$$

The minimum current $I_0$ needed to collect a beam of divergence $\alpha$ is given by

$$I_0 = \frac{\alpha^2}{(e/p)(\mu_0/2\pi)} \ . \tag{14}$$

The last parameter $r_p$ is derived from the envelope calculation. The envelope is the locus of the maximum amplitudes of the particle trajectories. Following the theory of the strong focusing systems, the amplitudes of an oscillation can be written as a function of the beam emittance $\varepsilon$ and of the $\beta$-function:

$$a = \sqrt{\varepsilon\beta} \ . \tag{15}$$

The emittance is the area of the phase-space ellipse and is a constant of the motion, it is expressed in metre.radian and can be evaluated, for instance, at the origin where the beam radius is $r_t$

$$\varepsilon = r_t\alpha \ . \tag{16}$$

The lens radius corresponds to the maximum value $\hat{\beta}$ of $\beta$

$$r_p = \sqrt{\varepsilon\hat{\beta}} \ . \tag{17}$$

The variation of the $\beta$-function along the beam axis is traditionally described by the $\sigma$-matrix

$$\sigma = \begin{pmatrix} \beta & \beta'/2 \\ \beta'/2 & (1 + \beta'^2/4)/\beta \end{pmatrix}, \tag{18}$$

$\beta'$ being the longitudinal derivative of $\beta$. Over a section defined by a

transfer matrix A, the σ-matrix varies from an initial value $\sigma_1$ to a final value $\sigma_2$:

$$\sigma_2 = A\ \sigma_1\ \tilde{A} \quad . \tag{19}$$

It is then a matter of algebra to find that the β-function reaches its maximum value inside the lens at a position

$$z = (\ell/2\varphi)\ \tan^{-1}\{\sin 2\varphi/[(r_t/r_e)^2 + \cos 2\varphi]\} \tag{20}$$

and that the radius $r_p$ is given by:

$$r_p^2 = \tfrac{1}{2}(r_t^2 + r_e^2) + \sqrt{\tfrac{1}{4}\left(r_t^2 + r_e^2\right)^2 - r_t^2 r_e^2 \sin^2\varphi} \quad . \tag{21}$$

The approximation of a point source, although it is unphysical because it assumes a zero emittance, has the great advantage of simplifying the formulae (21), (20) and (14) which become

$$r_p = r_e \tag{22}$$

$$z = \ell \tag{23}$$

$$I_p = I_0/\sin^2\varphi \quad . \tag{24}$$

Based on these simplified expressions, a first estimate of the lens parameters can be determined using the universal curves $(\ell\alpha/r_e)$, $(d\alpha/r_e)$ and $(I_p/I_0)$ plotted as a function of the phase φ (Fig. 4).

It is desirable in practice to operate the lens near π/2 to minimize the current. However, practical considerations impose a finite value of the ratio ℓ/d from which the operational phase can be deduced. In the case of the ACOL Project at CERN, the antiprotons are created by a 26 GeV/c proton beam which hits a target every 2.4 seconds. The proton beam contains $10^{13}$ particles equally shared between five short bunches of a 20 nanosecond duration each and separated by 104 nanosecond intervals. The time structure of the proton beam

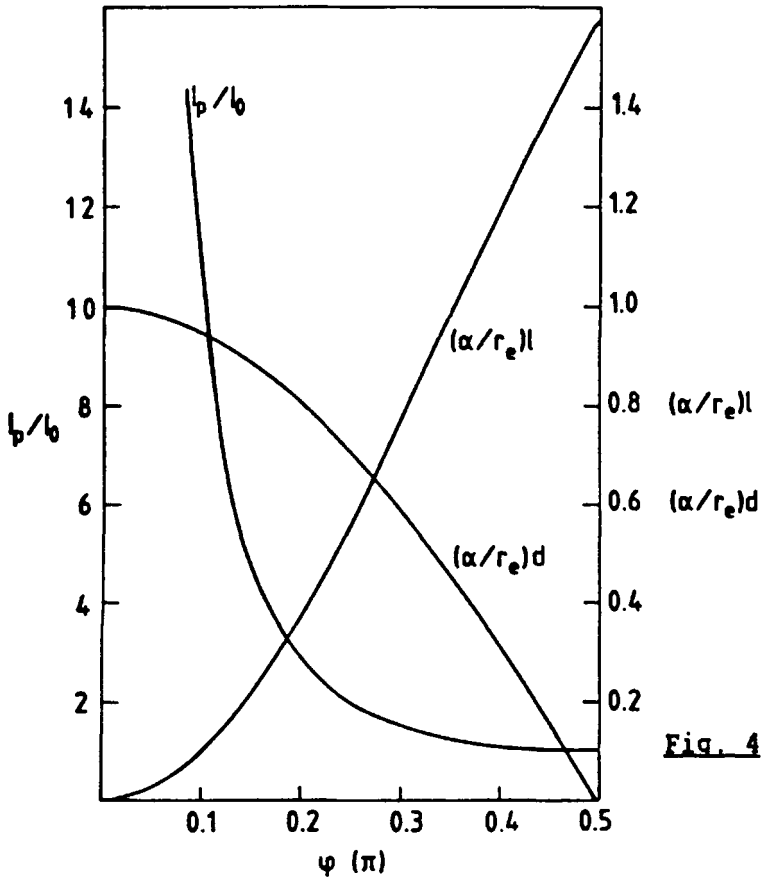


Fig. 4 - Variations of the normalized current, lens length and distance to target versus the oscillation phase.

applies to the antiproton beam and the plasma column must stay stable during 500 nanoseconds to allow not only the beam focusing but also reasonable tolerances on jitter and triggering. A typical set of parameters has been established using an iridium target whose downstream end is 110 mm distant from the entry to the plasma column. The target itself is 55 mm long and its diameter is 3 mm but the actual size of the antiproton beam cross section is twice as large and the beam divergence exceeds ±70 mrad slightly. The lens characteristics are:

$$I_p = 400\ \text{kA}, \qquad r_p = 21\ \text{mm}, \qquad \ell = 270\ \text{mm}, \qquad d = 150\ \text{mm}.$$

Under these conditions the number of collected antiprotons is estimated to be of the order of $1.3 \cdot 10^8$ per pulse. In the present configuration, target and lens are independent but it is conceivable to incorporate the target into the lens cathode to operate the lens at a plasma current closer to the ideal current.

The Dynamic Pinch

The theory of the dynamic pinch mechanism has been widely discussed[5-10]. Essentially three models have been conceived in order to explain the dynamics of the linear pinch. The first one[5] is the "snowplow" model in which the plasma current is assumed to be confined inside an infinitely thin shell. At the beginning, the current flows along the container wall where the inductance is minimum. Then, under the effect of the magnetic pressure, the shell moves quickly towards the lens axis sweeping up and capturing all the particles it encounters. When the collapsing plasma shell reaches the axis of the plasma column, it thermalizes, in a way which is not explained and produces the equilibrium pinch. Such a model, based on momentum conservation, provides no structure in space and suggests a singular infinite compression on the axis.

The second model is the "slug" model, due to D. Potter[6]. The formation of a shock, moving faster than the current shell, provides a means to justify the plasma thermalization, the equilibrium pinch formation, and gives information on the spatial distributions of the various relevant parameters of the equilibrium plasma. It assumes a pressure balance between the imploding plasma and the magnetic piston and a uniform pressure in the plasma layer between piston and shockwave. It predicts the shell motion and the final radius but it does not describe the radial oscillations of the plasma column after the implosion and the inertial effects are omitted.

In Miyamoto's model[10], the energy conservation in addition to the momentum conservation is made explicit and it leads to the "snowplow energy equation" from the classical MHD equations using an averaging technique over a cylindrical layer of finite thickness. The implosion phase and the following oscillatory phase are thus consistently described and the models that have

been mentioned previously turn out to be special cases of a general theory which has been used for describing the real plasma lens dynamics.

The plasma layer is enclosed between an inner boundary at radius $r_s$, the "shock-front", and an external boundary at radius $r_p$, the "magnetic piston". In this layer, the plasma is considered as a perfect gas and is described by the MHD equations. Moreover, the continuity condition is required for the mass, momentum and energy fluxes; the tangential component of the magnetic field is discontinuous if a surface current density exists. We assume a complete cylindrical symmetry and an infinite length of the pinch so that all quantities depend only on the radius r and the time t. The plasma beyond the shock front remains in the initial state until the shock front arrives and the plasma layer sweeps up all the ions. The mass density $\varrho$ is therefore equal to the initial density $\varrho_0$ for $r < r_s$ and is zero for $r > r_p$. The kinetic pressure p is $p_0$ for $r < r_s$ and is determined by the piston velocity for $r = r_p$.

The shock front propagates at the Alfven velocity

$$v_A = \sqrt{B_0^2/\mu_0\varrho_0} \tag{25}$$

where $B_0$ is the magnetic field produced by the discharge current $I_c$ at the wall radius $r_0$:

$$B_0 = \mu_0 \frac{I_c}{2\pi r_0} \quad . \tag{26}$$

The propagation time of the shock front from the wall to the axis is the Alfven time:

$$t_A = r_0/v_A \ , \tag{27}$$

and it must be synchronized with the time constant of the electrical circuit

$$t_c = \sqrt{LC} \tag{28}$$

where C is the capacity of the capacitor bank and L the total inductance composed of the external inductance $L_0$ and of the lens inductance $L_p$. The synchronisation is defined by the parameter

$$\nu = t_C/t_A \ . \tag{29}$$

In a semi-empirical way, the time $t_p$ at which the pinch occurs can be related to the geometric mean of $t_A$ and $t_C$:

$$t_p = k\sqrt{t_A t_C} \ , \tag{30}$$

the constant k depends on the synchronisation parameter $\nu$ and is equal to 1.5, 0.8 and 1.6 for the snowplow, slug and Miyamoto's models, respectively. For completeness, the acoustic wave can be taken into account; it propagates from the wall to the axis in a time

$$t_S = r_0/v_S \tag{31}$$

where the sound velocity $v_S$ is given by the formula

$$v_S = \sqrt{\gamma p/\varrho_0} \ , \tag{32}$$

$\gamma$ being the specific heat ratio. The importance of the acoustic wave is measured by the parameter

$$\lambda = \sqrt{\frac{2}{\gamma}\frac{t_C}{t_S}} \ . \tag{33}$$

In our case, the Alfven velocity exceeds the sound velocity by far and $\lambda$ is small. The quantities to be calculated are an average radius r characteristic of the plasma layer position, the plasma current $I_p$ and the voltage V at the terminals of the lens. It is convenient to introduce the reduced variables

$$x = r/r_0 \tag{34}$$

$$i = I_p/I_c \tag{35}$$

$$\tau = t/t_c \tag{36}$$

If the layer thickness is small as compared to r, which is true in the implosion phase, the snowplow energy equation can be written

$$\begin{aligned} \frac{d^2}{d\tau^2}\left[(1 - x^2)\,\frac{dx^2}{d\tau}\right] &= -\,4v^2\left\{\frac{i^2}{x}\cdot\frac{dx}{d\tau} + i\,\frac{di}{d\tau}\right\} - 4\lambda^2\,\frac{2-\gamma}{\gamma+1}\,\frac{dx}{d\tau} \qquad \tau < \tau_A \\ \frac{d^3x^2}{d\tau^3} &= -\,4v^2\left\{\frac{i^2}{x}\,\frac{dx}{d\tau} + i\,\frac{di}{d\tau}\right\} - 4\lambda^2\,\frac{2-\gamma}{\gamma+1}\,\frac{dx}{d\tau} \qquad \tau > \tau_A \end{aligned} \tag{37}$$

The other two equations are provided by the circuit dynamics:

$$\frac{d}{dt}\left[(L_p + L_0)I_p\right] + R_pI_p = V \tag{38}$$

$$C\,\frac{dV}{dt} + I_p = 0\ . \tag{39}$$

The lens inductance $L_p$ varies with time:

$$L_p = \frac{\mu_0 \ell}{2\pi}\,\ell n\left(\frac{R_0}{r_0 x}\right)\ , \tag{40}$$

$R_0$ being the radius of the return conductor. The time derivative $\dot{L}_p$ of $L_p$ is associated with the kinetic energy of the plasma layer whereas the term in $\dot{I}_p$ is related to the magnetic energy. All the problem of the lens design consists of converting the external energy $\frac{1}{2}CV^2$ into the highest magnetic energy $\frac{1}{2}L_pI_p^2$ and for this reason it is interesting to introduce the parameter

$$\xi = \frac{\mu_0}{2\pi}\,\frac{\ell}{L_0}\ . \tag{41}$$

The ohmic losses are

$$R_pI_p^2 = 2\pi\ell\int_{r_s}^{r_p} \eta j^2 r\,dr \tag{42}$$

where $\eta$ is the electrical conductivity.

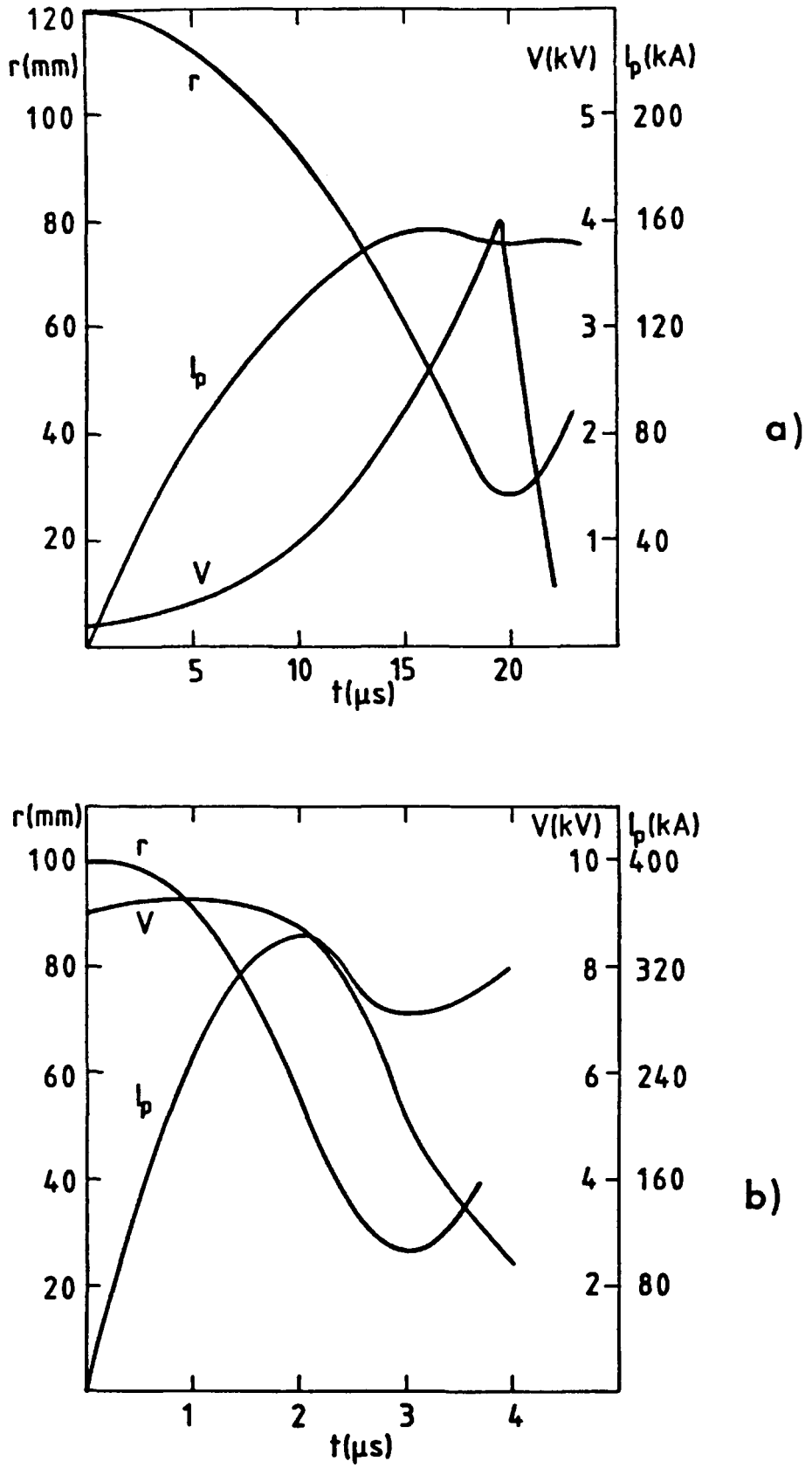


Fig. 5 - Theoretical pinch dynamics at low (a) and high (b) E regimes.

In Fig. 5 typical results of the numerical integration of eqs (37, 38, 39) are shown. Two regimes have to be distinguished. In the low $f$ regime, when the external inductance dominates, the current is quasi-sinusoidal. The voltage increases very rapidly because the pinch inductance rises during the plasma contraction. At a certain time the voltage has a peak. This time corresponds approximately to the time of maximum layer velocity, null acceleration, when the shock wave preceding the boundary of the plasma meets the axis. Later the voltage falls and a kink appears on the current waveform. When the voltage drops, the layer velocity comes to zero, changes sign and the pinch radius is minimum.

In the high $f$ regime (Fig. 5b), the current waveform is no longer sinusoidal, and the peak voltage disappears. In contrast with the low $f$ regime, the current intensity at the maximum contraction is strongly dependent on the $v$ value, and therefore on the initial voltage and pressure.

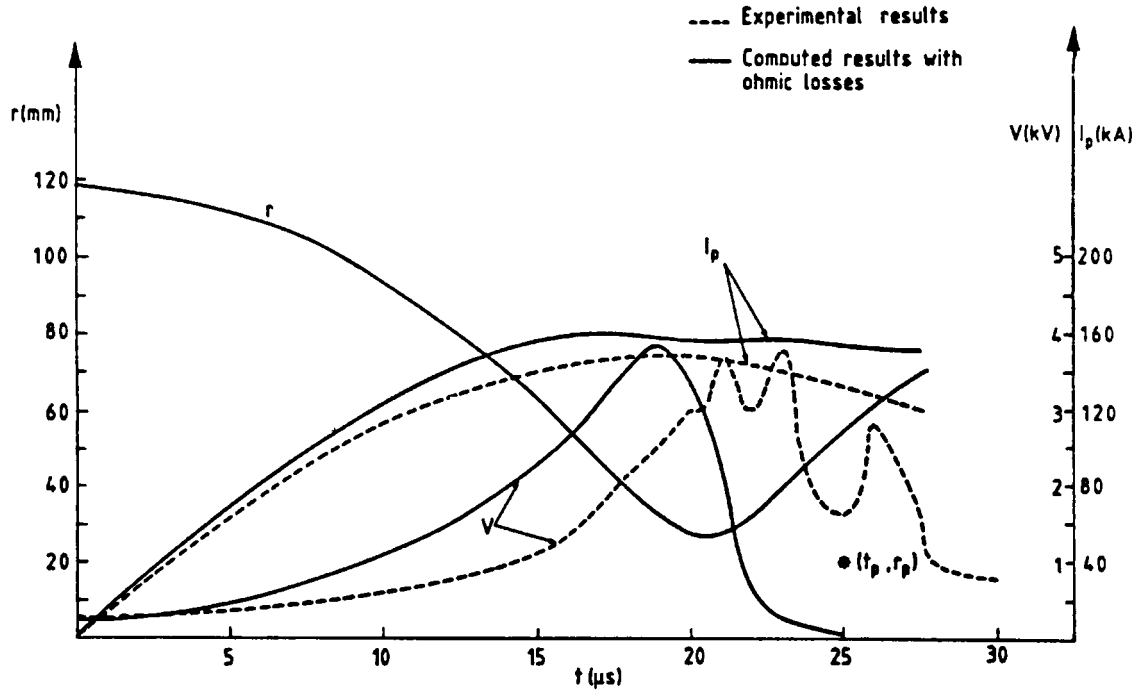


Fig. 6 - Comparison between numerical and experimental results for an argon discharge under a pressure of 40 Pa and at a charging voltage of 10 kV. The pinch radius and time (X) are deduced from magnetic measurements.

Plasma Lens Development and Experiments

The plasma lens application in an accelerator requires hollow electrodes (Fig. 7) to have free passage to the particle beam. The only absorbing elements in the whole plasma lens are the windows in the outside face of each hollow electrode. The geometry also improves the spatial and temporal stability of the dynamic pinch and the erosion rate of electrode material as it has been observed in other pseudo-spark devices[11-12].

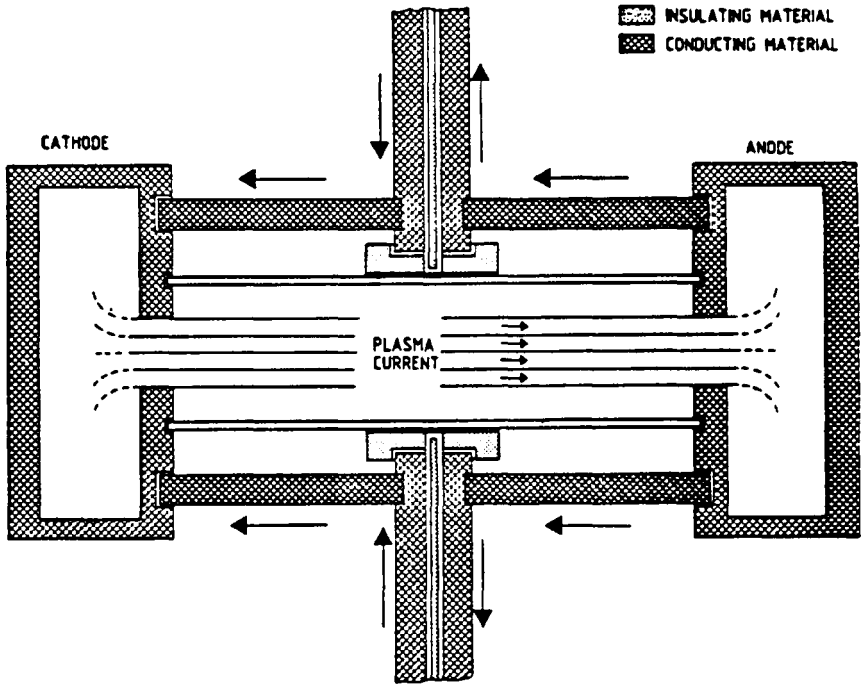


Fig. 7 - Plasma lens geometry.

The measurements described in this paper cover a wide parameter range of plasma lens dimensions, wall and electrode materials, gas type and pressures and current rise rates. They can be grouped into two classes:

a) Examination of pinch dynamics and magnetic field distribution by "single shot" experiments.

b) Study of long term behaviour under operational conditions.

Table 1 shows the plasma lens prototype characteristics. It is a rule in plasma physics experiments to consider the external electrical circuit as an integral part of the system. The basic scheme of the plasma lens pulse generator shown in Fig. 8 consists of one or more capacitor banks discharged via fast high current switches into the lens which can be characterized by a time-varying inductive and resistive load. Two pulse generators with the characteristics given in Table 2 were used in the measurements. They mainly differ by the external circuit inductance affecting the current rise rate.

Table 1 - Plasma Lens Prototype Characteristics

| PL Prototype No. | I | II | III | IV | V | VI |
|---|---|---|---|---|---|---|
| Length [mm] | 200 | 250 | 250 | 250 | 250 | 250 |
| Inner diameter of insulator $r_0$ [mm] | 40 | 236 | 190 | 185 | 190 | 180 |
| Insulator material | silica | silica or silica and metal rings | silica | $Al_2O_3$ or $Al_2O_3$ and graphite limiters | BN | AlN |
| Electrode material | steel | steel or tungsten | tungsten | tungsten | tungsten | tungsten |
| Electrode hole diameter [mm] | 20-25 | 30-40 | 40 | 40 | 40 | 40 |
| Gas type | He, Ar, Xe, $N_2$ | Ar, He, $N_2$ 50He-50Ar | Ar, He | Ar, He, $H_2$ | $H_2$ | $H_2$ |
| Gas pressure [Pa] | 3-2000 | 7-500 | 10-100 | 10-800 | 300-1100 | 300-1100 |
| Inductance [nH] at pinch diameter $d_p$ [mm] | 120 for $d_p$=3 | 95-130 for $d_p$=20-40 | 95-130 for $d_p$=20-40 | 95-130 for $d_p$=20-40 | 95-130 for $d_p$=20-40 | 95-130 for $d_p$=20-40 |
| Inductance at start of charge [nH] | 16 | 8.5 | 17.5 | 14.5 | 17.5 | 18 |

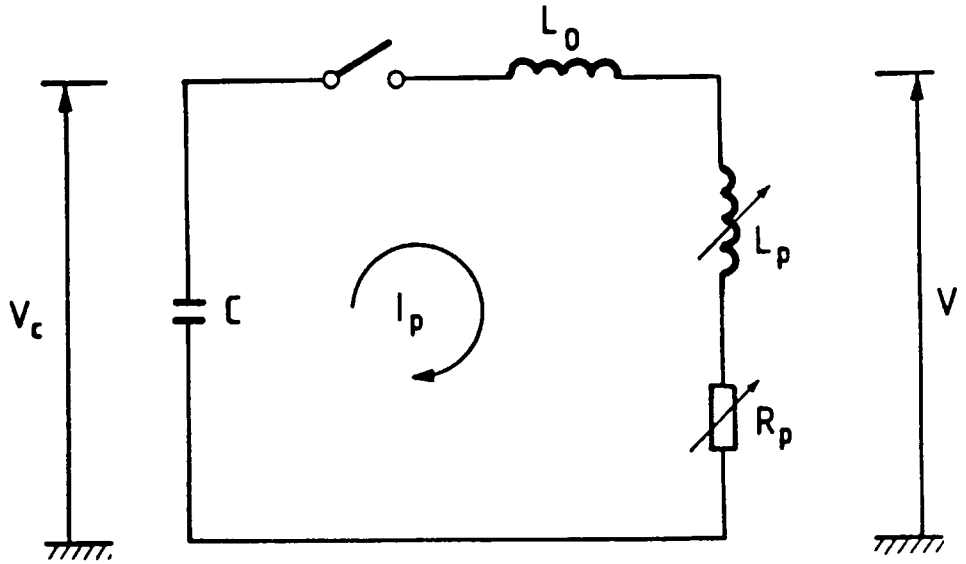


Fig. 8 - Electrical plasma lens circuit. $L_p$ and $R_p$ are the time dependent inductance and resistance of the plasma lens.

Table 2 - Characteristics of the Pulse Generators

| | | "Slow" | "Fast" |
|---|---|---|---|
| Total storage capacitance | [μF] | 281 | 108 |
| Nominal charging voltage | [kV] | 12 | 16 |
| Stored energy at nominal charging voltage | [kJ] | 20 | 14 |
| Maximal nominal current | [kA] | 190 | 500 |
| Initial dI/dt at nominal current | [$A.s^{-1}$] | $1.3 \cdot 10^{10}$ | $6 \cdot 10^{11}$ |
| Circuit inductance | [nH] | 700 | 10 |
| Half-cycle time | [μs] | 45 | 7.5 |
| Repetition time | [s] | Single shot | 2.4 (max.) |

An overview of the measurements is given in Table 3. With both pulse generators the current rise rate could be varied by changing the charging voltage.

Table 3 - Overview of Tests with Different Plasma Lens Prototypes

| Pulse generator | "Slow" | | "Fast" | |
|---|---|---|---|---|
| PL-prototype No. | I | II | II, IV | III, IV, V, VI |
| Measurements | u(t),i(t), streak + framing photography | u(t),i(t), magnetic field | u(t),i(t), light output on axis, magnetic field | u(t),i(t), light output on axis, long term tests |

The aim of the "single shot" measurements was the study of pinch dynamics, stability of discharge and azimuthal magnetic field distribution. Streak and framing photography were only performed on prototype I at slow current rise. Although fast photography can only give a qualitative picture of the current distribution, it is a valuable means to check spatial and temporal stability of the pinching plasma column. From voltage and current waveforms the pinch times and the discharge reproducibility can be accurately measured. The simple measurement of the light output on the plasma lens axis by a photodiode is also a valuable tool to determine the collapse time of the plasma shell.

In the context of a particle collector lens the magnetic field measurements are essential. They deliver also information about current and current density distribution, which define the pinch dynamics. Two screened coils of 0.5 mm diameter and 0.5 mm length were inserted radially through the insulator wall into the discharge plasma. From a series of 20 to 30 shots the field distributions B(r,t) can be quantitatively composed. Comparison of the signals of both coils give an indication of discharge symmetry.

Since the ACOL plasma lens is pulsed every 2.4 seconds for at least 1.5 million pulses without interruption, the measurements of the deterioration of electrodes and insulator tubes are essential. Evaporation rates of different

insulator materials were determined by weight loss measurements or by the increase of internal tube diameter. Erosion rates can best be estimated from the geometrical change of the electrode shape. The mechanisms of surface erosion and evaporation were studied with electron microscopy.

The plasma dynamics in the various types of lenses differed substantially in the slow and the fast pulse generator. In Fig. 9a) and b) voltage and

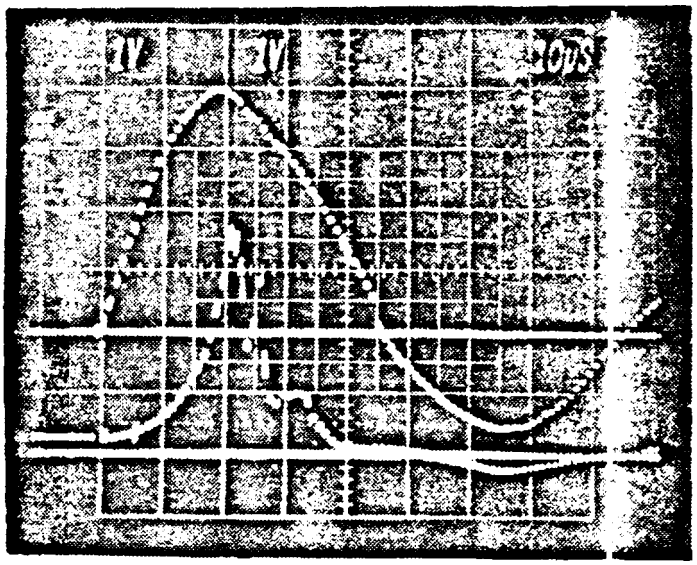

a)
Charging voltage: 10 kV
Gas : argon, 40 Pa
Current : 37 kA/div
Voltage : 1 kV/div
Timescale : 10 µs/div

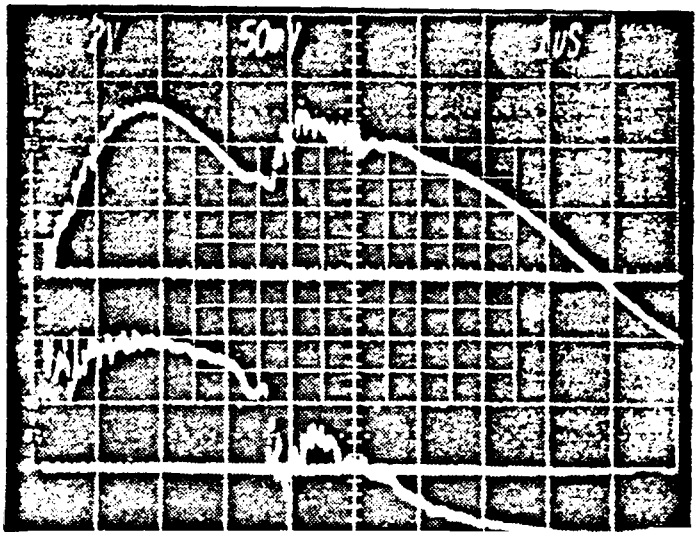

b)
Charging voltage: 16 kV
Gas : hydrogen, 400 Pa
Current : 167 kA/div
Voltage : 2 kV/div
Timescale : 1 µs/div

Fig. 9 - Current (upper trace) and voltage (lower trace) waveforms for a slow (a) and fast (b) pulse generator.

current waveforms of the plasma lens are shown for slow and fast current rise times. In both cases the maximum contraction of the plasma column leads to a rise in voltage followed by a sharp fall and to a kink in the current waveform. Streak photographs obtained with prototype PL-I showed excellent temporal and spatial stability with argon and xenon even beyond the first contraction phase (Fig. 10). The pinch time and the minimum pinch radius were

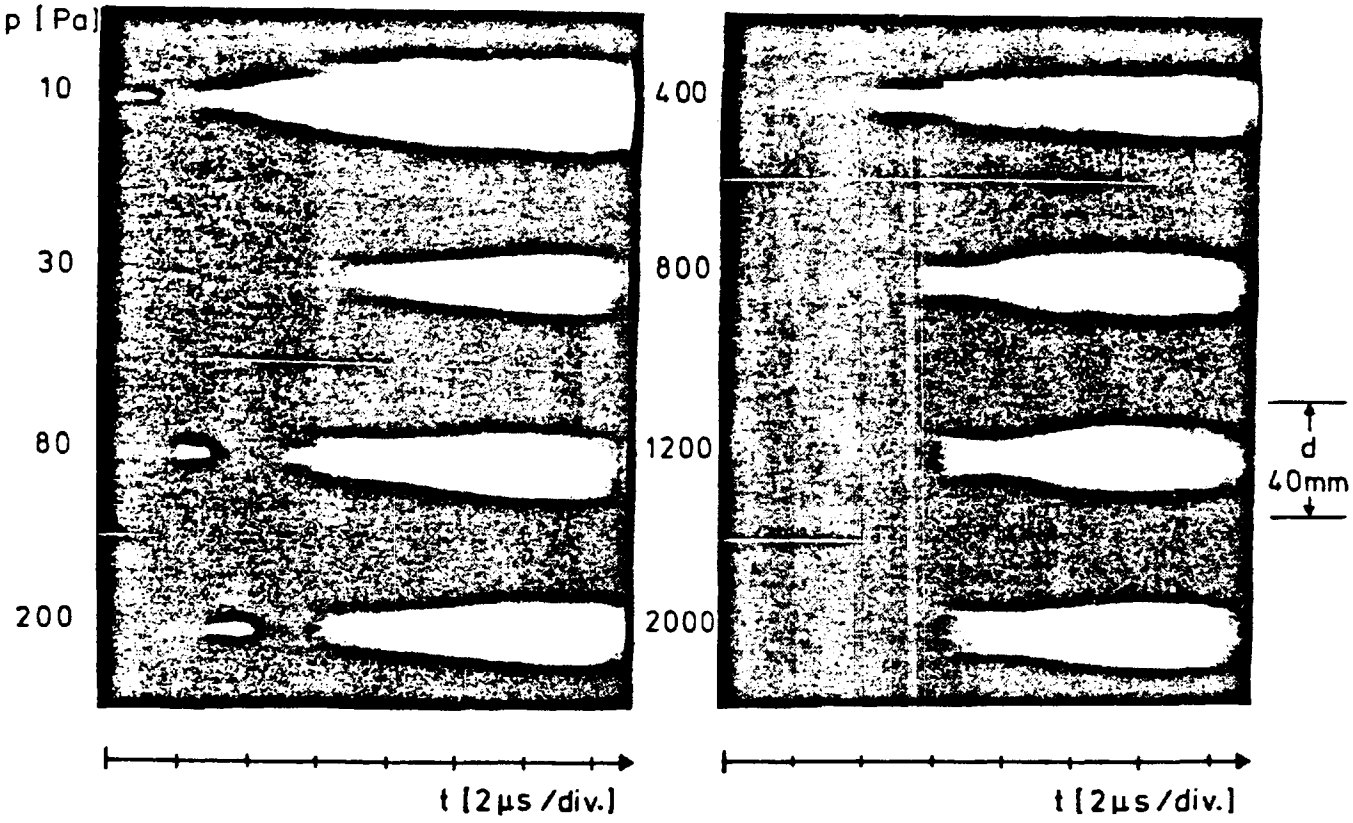


Fig. 10 - Streak photographs of argon discharges at different pressures (charging voltage = 9 kV).

determined as functions of initial pressure (Fig. 11), current rise rate and atomic weight of the filling gas. The scaling laws derived from the snowplow model proved to be valid over a limited parameter range for the prototypes PL-I and II at low current-rise rates.

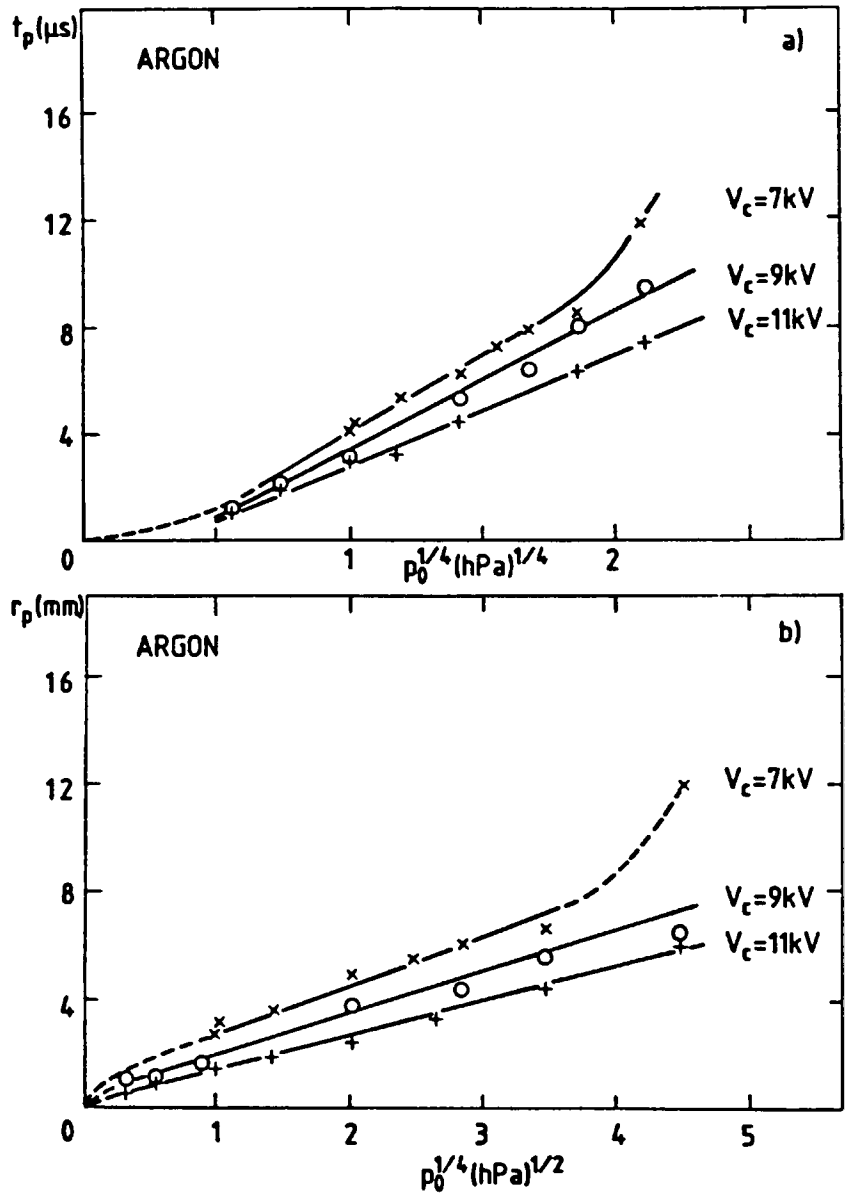


Fig. 11 - Scaling laws of pinch time (a) and radius (b) as a function of the initial pressure $p_0$ deduced from streak photographs.

The measurements of magnetic field distribution $B_\varphi(r,t)$ in the prototype PL-II with the slow generator confirmed that the plasma dynamics followed closely the rules of a pure z-pinch. Instabilities appeared only a few microseconds after the first contraction. During the pinch phase the current density is concentrated within a radius of 20 to 25 mm (Fig. 12) and is sufficiently uniform to produce a good field linearity.

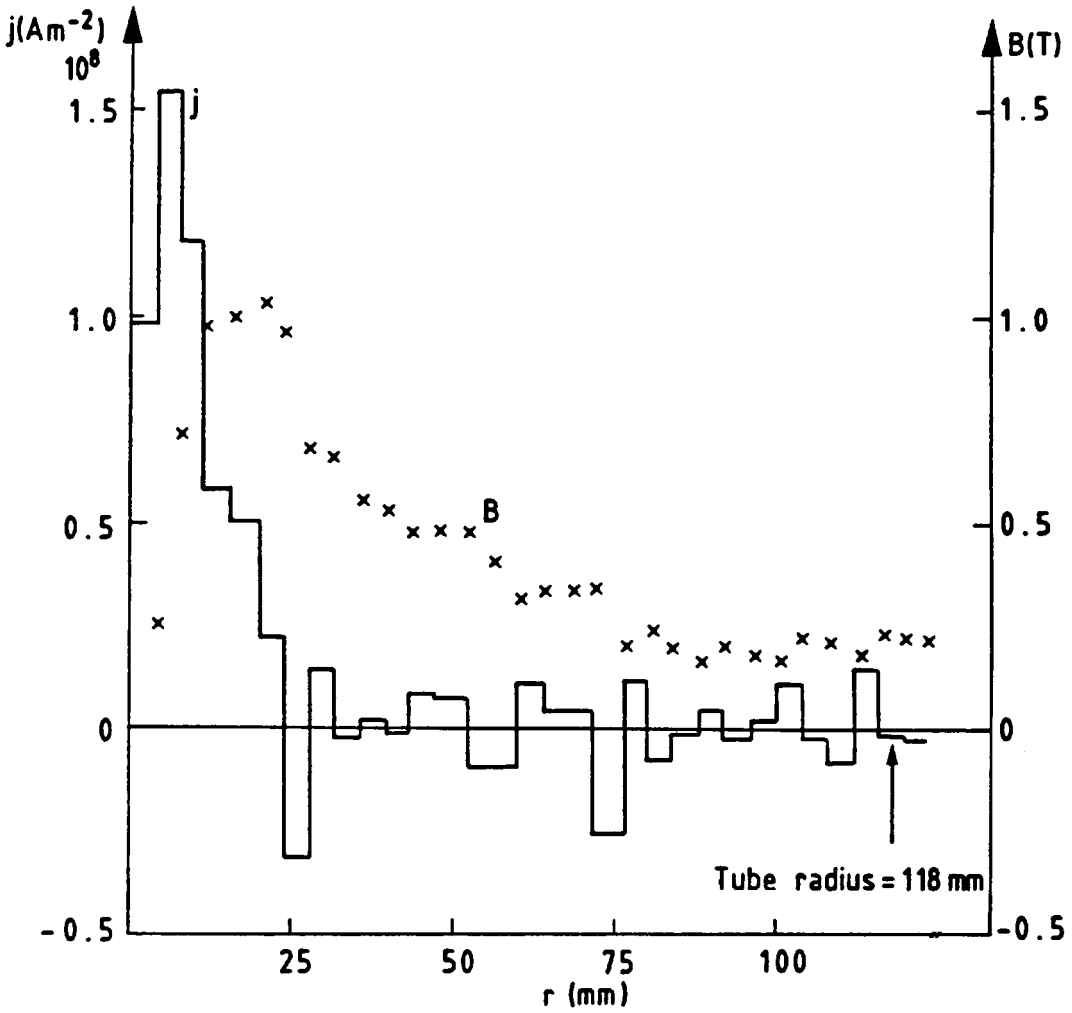


Fig. 12 - Measured magnetic field B and calculated current density j 25 μs after ignition as a function of radius. Charging voltage: 10 kV, pressure: 40 Pa, Ar.

The pinch dynamics in the plasma lens proved to be much more complex with the fast pulse generator. Strong wall currents may occur during or even before the main contraction phase. The appearance of a wall current increases with higher current rise times and with lower gas pressures. Heavier gases, like Ar and $N_2$ but also He, always lead to strong wall currents. The characteristics of the insulator wall material also influence the development of wall currents. A typical current distribution derived from magnetic field measurements is shown in Fig. 13 for a PL-II-type silica tube filled with Ar. A strong crowbarring effect is exerted on the pinch current by the surface

current, which reaches nearly 80% of the total current. Hence, the magnetic field amplitudes in the central plasma column remain very low.

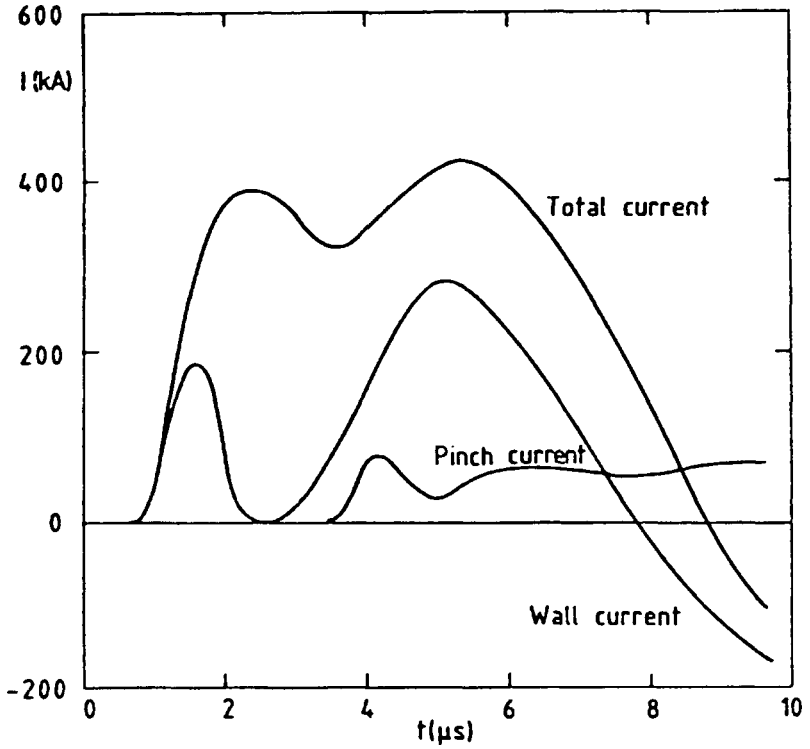


Fig. 13 - Current distribution in an argon discharge under 25 Pa pressure and at 15 kV charging voltage. The container is a silica tube.

With hydrogen at high pressure (>5 mb) wall currents may be suppressed Fig. 14). During the pinch, all the current flows in the central plasma column and the magnetic field reaches a high value. At low hydrogen pressure the wall current formation reappears. The influence of the gas type on the pinch dynamics is mainly related to radiation processes. Argon plasmas are highly radiative, whereas the less radiating hydrogen plasmas are much hotter. This phenomenon can also be deduced from the light output measurements and from the damping decrements of the current waveform oscillations. The influence of the different insulator wall materials seems to be mainly determined by their thermal properties like dissociation temperature $T_c$ and heat conduc-

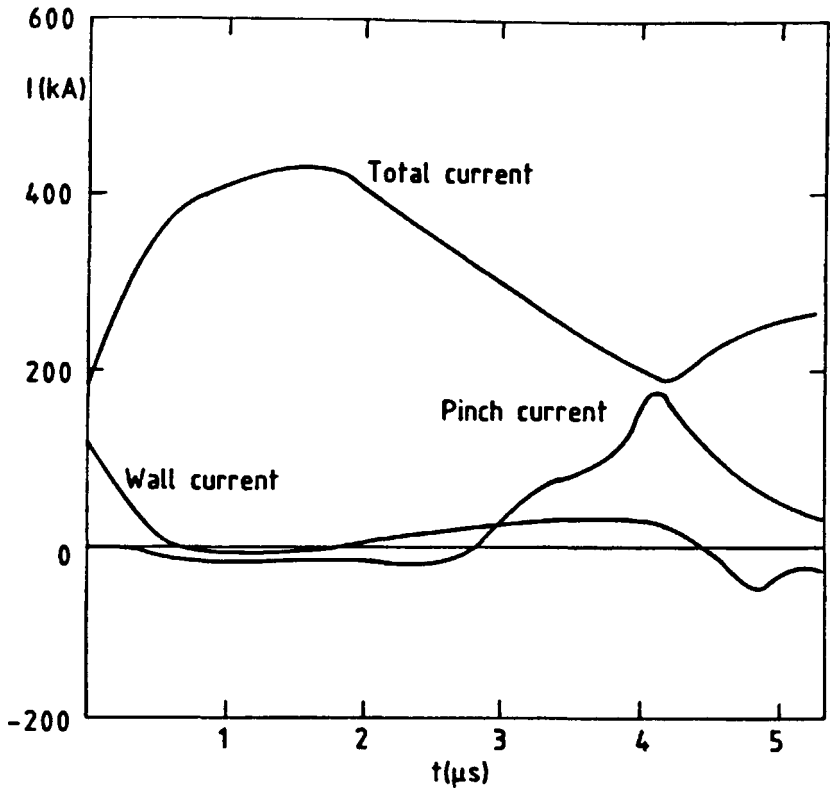


Fig. 14 - Current distribution in a hydrogen discharge under 800 Pa pressure and at 15 kV charging voltage. The container is an alumina tube.

tivity k. The materials which evaporate more induce strong wall currents. The wall currents in silica start earlier and are at least twice as strong as in an $Al_2O_3$ tube. Using a thermal quality factor $q = T_C \sqrt{\rho k c}$ ($\rho$ = density, c = heat capacity)[13], one can classify the wall materials (Table 4). The higher the q-value the better the material withstands the heating due to the plasma or to the radiation. Such a classification, however, is only indicative because some characteristics may dramatically vary with temperature.

Table 4 - Thermal Quality Factor q for Some Materials ($q/W.m^{-2}.s^{1/2}$)

| | | | |
|---|---|---|---|
| Diamond | >1000 | Aluminium oxide | 85 - 150 |
| Graphite | 400 - 500 | Silicon nitride | 90 - 150 |
| Tungsten | 430 - 480 | Silica | 16 - 35 |
| Aluminium nitride | 140 - 340 | Pyrex | 7 - 8 |
| Boron nitride | 150 - 250 | Glass | 2 - 4 |

Several long term tests (Table 5) performed with different materials confirmed the usefulness of the quality factor q. The number of pulses in the long term tests varied between 20 000 and 150 000. The highest evaporation rates were found with silica. A significant improvement was obtained with $Al_2O_3$ and with boron nitride. Comparative measurements of evaporation rates with argon and hydrogen proved the enhancing role of strong wall currents. Electron microscopy showed no evidence of ion sputtering process, which become important only above ion energies of 30 eV.[14] Wall heating, chemical erosion, material dissociation and evaporation seem to be the main damaging mechanisms.

Table 5 - Results of Long Term Tests

| PL-Type | III | | IV | | | V | VI |
|---|---|---|---|---|---|---|---|
| Insulator material | $SiO_2$ | | $Al_2O_3$ | | | BN | AlN |
| Remarks | Air cooling | Water cooling | | With graphite limitors | | Oil cooling | |
| $V_c$ [kV] | 16 | 16 | 16 | 16 | 16 | 16 | 16 |
| $i_{peak}$ [kA] | 400 | 400 | 400 | 400 | 400 | 400 | 400 |
| Gas-type | Ar | Ar | Ar | Ar | $H_2$ | $H_2$ | $H_2$ |
| Total weight loss [g] | 730 | 400 | 95 | 65 | 10 | 22 | 686 |
| Weight loss per shot [mg] | 7.3 | 7.7 | 4.7 | 3.2 | 0.1 | 1 | 22.9 |
| Evaporated wall layer per shot [nm] | 23 | | 8.4 | 5.7 | 0.17 | 3.4 | - |

The electrode erosion rate is much lower than the evaporation rate of the insulator wall material. Moreover, the electrode material is a tungsten alloy with a melting temperature of only 1450°C. For the lifetime of a plasma lens electrode erosion seems therefore a negligible problem.

The real long-term problem in a plasma lens is the deposition of evaporated material on electrodes and beam windows. Silica is especially bad in this respect. After evaporation, alumina is mainly transformed into powder, which could be blown out from time to time. A very good candidate is boron nitride. This material in hydrogen not only has a low evaporation rate, but the evaporation products are almost fully transformed into gases, e.g. $N_2$, $NH_2$ and $(BH_3)_2$, which are pumped away. No contaminating or conducting deposits are left.

Experience with aluminium nitride has been disappointing. However, the test with AlN is not relevant to the quality factor because distinct conductive discharge channels were found on the inner tube wall which took over almost the full total current. The strong evaporation came uniquely from these spark channels whereas the smooth tube surface, which was exposed to the normally pinching plasma for almost half the time of the long term test, did not show any measurable evaporation. Nevertheless, the test with AlN and $H_2$ shows a danger of wall contamination with aluminium, which is produced by dissociation of AlN and which is not transformed into a volatile product.

## Discussion of the Results

The experiments performed on plasma lens prototypes revealed many potential problems which may jeopardize the operation of a plasma lens under conditions like those valid in the ACOL target area. One of the main traps to avoid is the wall current bypassing the current through the pinched column. Gas

types like $H_2$ or $D_2$, which emit little radiation, are particularly well suited to eliminate wall currents, especially at high current rise rates. The insulator wall material is decisive for the long term behaviour of a plasma lens. A plasma lens requires materials with optimal thermal properties, e.g. high heat conductivity, high heat capacity and high dissociation temperature. Moreover, the evaporation products should be volatile so that they can be pumped away without obstructing electrodes or parts of the insulating cylinder; boron nitride has this property. The additional use of graphite limiters may reduce the material evaporation by more than 30%.

Besides gas type and wall material the current rise rate proved to be a very important parameter. The limits of energy input into z-pinches for fusion application have been recognized already earlier[15]. The faster the pinch and the faster the plasma lens inductance changes, the smaller is the amount of magnetic energy which becomes available. The mechanical energy is mostly converted into plasma heating and radiation. Only small fractions may be transferred back into the magnetic pinch energy by the formation of "inductons"[16] which are current loops excited after interaction between reflected shock waves and magnetic piston.

Oscillograms of the field variations with time at given radial positions are displayed in Fig. 15. The case of Fig. 15a corresponds to the conditions of Fig. 14; the pinch occurs on the descent of the current waveform; the full intensity of 200 kA flows through the pinch and the field reaches the expected value of 2 T at the pinch radius of 20 mm. When the pinch is synchronized by lowering the pressure (Figs. 9b and 15b), the current is slightly augmented (230 kA), the field measured at 10 mm is 3.4 T and is consistent with a pinch radius of 12 mm where the field would be 3.8 T. For the ACOL application, the field should be 4 T at 20 mm; we have therefore not yet tested a satisfactory

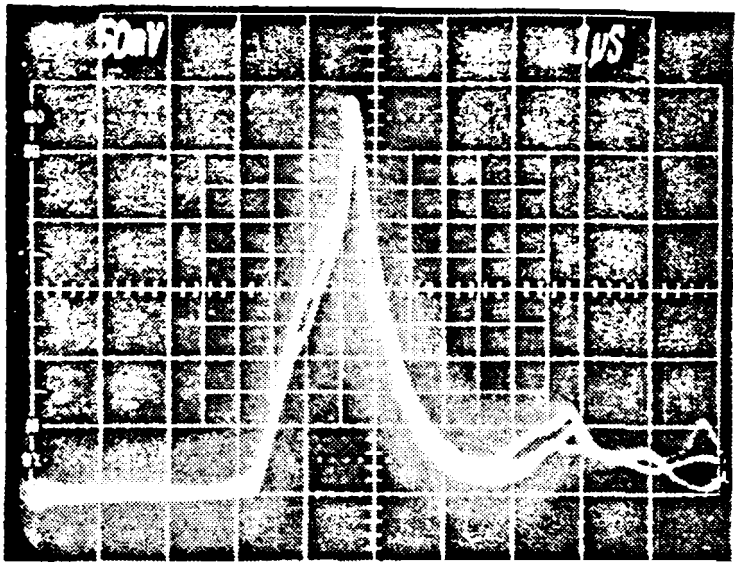


a)

Charging voltage: 15 kV
Gas : hydrogen, 8 mb
Radius : 20 mm
$B_{max}$ : 2 T

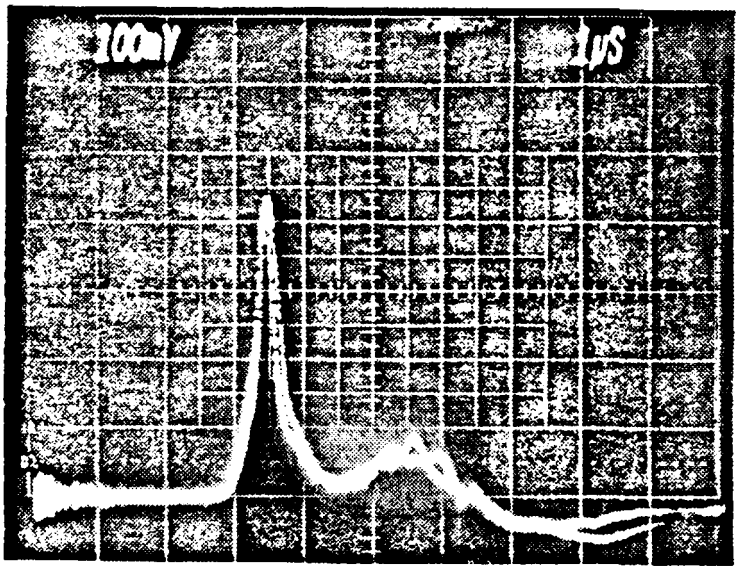


b)

Charging voltage: 15 kV
Gas : hydrogen, 4 mb
Radius : 10 mm
$B_{max}$ : 3.4 T

Fig. 15 - Field variation with time in a hydrogen pinch.
Vertical scale: 130 mV/Tesla.

set of parameters. Furthermore, the third specification which concerns the pinch duration is not fulfilled either: the field levels which have been quoted are peak values, the mean values over 500 ns are lower. If the design performances are not yet obtained, the present performances can be improved since five parameters: charging voltage and capacity, gas pressure and atomic weight, initial radius, are at hand to control three variables: pinch radius

pinch radius, pinch duration and field level. The final solutions would require a pulse generator with a slower rise time.

## Conclusion

The appeal of a plasma lens as a focusing device of large divergence particle beams lies in its transparency: the focused particles are not absorbed, the plasma current can be adjusted near its optimum value and the plasma remains unaltered in a highly radioactive area. The experience developed on the ACOL project has confirmed the quality of the z-pinch models for relatively slow implosions. When the implosions are fast, radiative processes play an important role especially in the build-up of wall currents and the predictions become uncertain. A positive result obtained in the study of plasma-wall interactions is the selection of resistant wall materials like alumina or boron nitride which should ensure a long life time. The so far attained performances do not yet fit exactly the design parameters but the parameter set for an operational plasma lens can be easily established by a moderate extrapolation from the tested prototypes.

## References

1. W.K.H. Panofsky, W.R. Baker, Rev. of Sci. Instr. 21, (1950) 445.
2. E.B. Forsyth, L.M. Lederman, J. Sunderland, IEEE Trans. Nucl. S ci. 12, (1965) 872.
3. J. Christiansen, K. Frank, H. Riege and R. Seeböck, CERN/PS/84-10 (AA), (1984).
4. L. De Menna, G. Miano, B. Autin, E. Boggasch, K. Frank, and H. Riege, CERN/PS/84-13 (AA), (1984).
5. M. Rosenbluth et al., Los Alamos Scientific Lab. Rep. LA-1850 (1954).

6. D. Potter, Nucl. Fusion 18, (1978) 813.

7. J.E. Allen, Proc. Phys. Soc. 70, (1957) 24.

8. S. Lee, Plasma Physics 25, (1983) 571.

9. S. Lee, J. Phys. D: Appl. Phys. 16, (1983) 2463.

10. T. Miyamoto, Nucl. Fusion 24, (1984) 337.

11. D. Bloess et al., Nucl. Instr. and Methods 205, (1983) 173.

12. E. Boggasch, V. Brückner and H. Riege, Proc. of the 5th Pulsed Power Conf., Arlington, (1985) 820.

13. J.A. Phillips, J.L. Tuck, Proc. of the 2nd UN Int. Conf. on the Peaceful Uses of Atomic Energy, Vol. 32, Geneva 1958.

14. Sputtering by Particle Bombardment (Topics in Appl. Phys., V. 47), R. Behrisch, Springer Verlag Berlin Heidelberg New York (1981).

15. H.A.B. Bodin et al., Nucl. Fusion 1, (1960) 54.

16. I.Y. Butov, Y.V. Matveev, Sov. Phys. JETP 54, (1981) 299.